International Journal of Rock Mechanics & Mining Sciences 195 (2025) 106297

Contents lists available at ScienceDirect

International Journal of Rock Mechanics and Mining Sciences

journal homepage: www.elsevier.com/locate/ijrmms

Evolution of fracture network, permeability and induced seismicity during fatigue hydraulic fracturing

Chang Xia [a], Huanyu Wu [a], Ki-Bok Min [b], Derek Elsworth [c], Qi Zhao [a,*]

[a] Department of Civil and Environmental Engineering, The Hong Kong Polytechnic University, Hong Kong, China
[b] Department of Energy Resources Engineering and Research Institute of Energy and Resources, College of Engineering, Seoul National University, Seoul, Republic of Korea
[c] Department of Energy and Mineral Engineering, EMS Energy Institute and G3 Center, The Pennsylvania State University, PA, USA

ARTICLE INFO

Keywords:
Cyclic hydraulic fracturing
Fatigue damage
Induced seismicity
Permeability
DEM modeling
Hydromechanical modeling

ABSTRACT

Cyclic hydraulic fracturing (CHF) shows potential in reducing induced seismicity compared to conventional hydraulic fracturing (HF). However, controlling mechanisms that potentially limit induced seismicity but still enhance permeability during CHF remain unclear. We develop a novel time- and stress-dependent damage representative of fatigue crack growth through a coupled hydromechanical model using the block-based discrete element method (DEM). This new framework addresses the challenges in modeling CHF by simultaneously considering discrete fracture network, hydromechanical coupling, fatigue and in-situ stresses. Matching pressurization cycles-to-failure data in laboratory experiments confirms the contribution of sub-critical crack growth in the reduced breakdown pressures in CHF. Modeling fluid injections into a fractured reservoir with contrasting far-field stress ratios of 1.17 and 1.40 shows that CHF mainshocks are smaller than those by conventional HF. While HF induces seismicity primarily through the creation of new fractures, CHF generates seismicity predominantly from multiple small shear reactivations – these dissipate energy progressively and thereby reduce mainshock magnitude. CHF enhances permeability by creating a more connected fracture network than HF. Far-field stress ratio influences permeability by directing fracture growth orientations, and larger stress ratio leads to a higher proportion of shear fractures. This study provides new quantitative insights into the mechanisms of CHF in reducing induced seismicity while increasing effectiveness in elevating permeability.

1. Introduction

Hydraulic fracturing (HF), also referred to as hydraulic stimulation or fracking, has been extensively employed since the 1940s to improve reservoir permeability for subsurface energy extraction.[1,2] In recent years, HF has also emerged as a crucial technique in optimizing the recovery of deep geothermal energy resources and potentially geological carbon sequestration.[3–5] This process involves the injection of pressurized fluids into reservoirs, resulting in the development of transmissive fracture networks that consist of both newly-formed and pre-existing fractures.[6] While HF offers significant benefits, it also poses risks, such as the potential to induce or trigger large events, which may cause economic damage and elicit public concern.[7–11] For example, one geothermal project in Basel, Switzerland, was discontinued due to earthquakes caused by fluid injection.[12] Similarly, the Pohang earthquake in South Korea, the most destructive in the region since 1905, was linked to fluid injection from a nascent enhanced geothermal system.[13]

Breakdown pressure (P_b) defines the rupture pressure at the borehole wall and is influenced by rock properties, field stress, and fluid pressure. P_b at depth generally increases as in-situ stresses increase. Similarly, the need to develop or reactivate a penetrative fracture network requires large fluid injection volumes to reach far from the well. Thus, the goal of hydraulic stimulation design is to devise an advanced injection scheme that can control fracture propagation while simultaneously minimizing undesired seismicity.[14] Fatigue hydraulic fracturing, also commonly referred to as cyclic hydraulic fracturing (CHF) or soft stimulation, is one such strategy to optimize the development of fracture networks.[15–20] Unlike conventional HF, which uses continuous injection, CHF employs cycled high- and low-injection pressures.[21] Cycled pressures at incipient fracture tips promote fatigue fracturing,[22,23] driving fracture tips at a peak fluid pressure (P_p) lower than the HF P_b and potentially reducing seismicity.[24,25] Laboratory observations have demonstrated the

This article is part of a special issue entitled: CouFrac 2024 published in International Journal of Rock Mechanics and Mining Sciences.

* Corresponding author.
E-mail address: qi.qz.zhao@polyu.edu.hk (Q. Zhao).

https://doi.org/10.1016/j.ijrmms.2025.106297
Received 3 August 2025; Received in revised form 26 September 2025; Accepted 1 October 2025

advantages of CHF in reducing P_b by 20 % for Pocheon granites,[25] 25 % for shale[26] and 16 % for sandstones.[27] Numerical,[15] experimental[28] and field[19,29] studies have also shown that CHF lowers the magnitude of individual seismic events compared to HF.

Conversely, the effectiveness of CHF in increasing permeability compared to conventional HF remains inconclusive. Some studies suggest that CHF enhances permeability due to the formation of extensive fracture networks.[27,30,31] For instance, Zimmermann et al. reported that in-situ experiments in the Äspö Hard Rock Laboratory in Sweden demonstrated a 12.5-fold increase in permeability with CHF compared to HF.[3] However, observations by Hofmann et al., indicate from one of the hydraulic stimulations in Pohang (Korea) that permeability increases achieved through HF are merely comparable to those of CHF.[19] While in-situ stress is known to influence seismicity induced by HF,[32] its impact during CHF remains undefined. Furthermore, the characteristics of seismicity during CHF, particularly the rate of energy release, remain ill-constrained. Some studies suggest that CHF involves a combination of mechanical fatigue and fluid infiltration.[33] During CHF stimulations, injection pressure is periodically lowered to enable stress relaxation,[25] with a significant portion of the hydraulic energy converted into aseismic rock damage and fracturing.[22]

Although numerical simulations offer a viable alternative to field tests, a comprehensive model that accurately represents the CHF process is still lacking. Capturing the CHF process requires a comprehensive approach that considers hydromechanical coupling, fatigue damage evolution under subcritical stress, fracture propagation, and induced seismicity.[15,34–37] Various numerical methods have been employed to simulate hydraulic fracture growth, by using both continuum-based and discontinuum-based models. Continuum-based models include several approaches such as, finite element methods (FEM),[38] extended finite element methods (XFEM),[39] discontinuous deformation analysis,[40] boundary element methods (BEM),[41] phase field methods,[42–45] peridynamics[46] and numerical manifold methods.[47] However, these models often struggle to accurately mimic the mechanistic and geometric complexity of fracture networks.[48] They typically assume tensile failure as the primary mode, whereas experimental observations frequently record shear-type seismic events, and in some cases, shear failure predominates.[36,49,50] To address these limitations, discontinuum-based methods such as the discrete element methods (DEM)[15,51–53] and the combined finite-discrete element method (FDEM)[54,55] have been utilized. These methods are better suited for modeling complex hydraulic fracture growth in rock masses with multiple pre-existing fractures, flaws or joints. For example, Wasantha and Konietzky used block-based DEM to investigate the reactivation of fractures and their subsequent effects on reservoir properties during hydraulic stimulation.[56] Additionally, Zangeneh et al. and Zhao et al. considered the effect of natural fractures and the in-situ stress on hydraulic fracture propagation using block-based DEM.[57,58]

To date, several attempts have been made to simulate fatigue hydraulic fracturing. For instance, Zang et al. employed DEM to model fatigue hydraulic fracturing under multi-stage fluid injection,[15] where the P_p increased progressively at different stages, however, fatigue damage evolution was not considered. Xi et al. modeled CHF using a continuum-based fracture model,[59] where the CHF is conducted in one cohesive crack. Additionally, Zhu and Dong simulated CHF via particle-based DEM by simultaneously considering stress corrosion and hydromechanical coupling.[35] However, there are limitations for these models: firstly, when rocks undergo severe damage or significant changes in pore geometry, particle-based DEM struggles to distinguish between pores and pore throats.[36] Thus, the reactivation of, and fluid leak-off from, fractures cannot be modeled – thus any fracture reactivation that may induce seismicity cannot be captured. Furthermore, particle-based DEM typically uses rigid blocks to represent the rock mass, simplifying local rock stress to a force-displacement relationship applied only at contact points.[60] Unfortunately, this necessary simplification makes it challenging to account for subcritical stress states in particles for mechanical fatigue calculations. These challenges highlight the need for more advanced modeling techniques that can accurately capture the complexities of CHF.

We address these limitations by developing a new hydromechanical damage model using block-based DEM to simulate the key processes that define CHF. This new model is first calibrated and validated against laboratory observations before benchmarking a block scale demonstration specifically contrasting the response between traditional HF and CHF, where pre-existing discrete fracture networks (DFN) are an implicit characteristic. We specifically explore the effects of different horizontal-to-vertical in-situ stress ratios (K-ratios) on fracture network propagation, induced seismicity, and permeability enhancement for CHF. We use these observations to define key mechanistic controls that differentiate CHF from HF in mitigating induced seismicity, maintaining permeability growth and thus optimizing efficiency.

2. Hydromechanical damage model

2.1. Discrete element method

A two dimensional discrete element method (DEM)[61] is used to simulate the response of rock subjected to continuous and cyclic hydraulic injections. Voronoi tessellation is utilized to generate a heterogeneous distribution of element blocks (Fig. 1a).[62–65] The Voronoi boundaries are generated iteratively, guided by the average edge length l of blocks and an iteration parameter n. We set the ratio of l to the model length at 2×10^{-2} (dimensionless) and n at 200 with consideration of the competing needs of computing efficiency and model granularity. Pre-defined faults/fractures (discontinuities) of varying orientation, persistence, and spacing are distributed on the Voronoi block boundaries. Block-block contacts are identified via corner-to-edge or edge-to-edge interactions. Each single block is further discretized into triangular (finite) elements, where elastic deformation is linearly elastic. The Mohr-Coulomb failure criterion is employed at contacts as cohesive bonds before failure, with fracture growth explicitly followed by the rupture of such contacts (Fig. 1b).[66] As a result, rupture occurs under local stresses that exceed strength (Fig. 1b). Although strengths are deterministic, the parameters that govern block-deformation and breakage of contacts are micromechanically-localized and must be calibrated against macroscale observations.[67]

2.2. Coupled hydromechanical simulation

In DEM, hydromechanical coupling is typically achieved by constructing pore networks where flow pathways link "pores" at pathway intersections.[15,36,52,68] In our study, the pore (conductive fracture) network is generated along block contacts (Fig. 1c) with the cubic law[57,69] adopted to define an effective permeability/transmissivity. Each contact is composed of several sub-domains separated by length L to calculate the pressure gradient (i.e., P_1 and P_2 represent the fluid pressures of domains 1 and 2, respectively). Thus, the pressure gradient between contacting domains 1 and 2 is expressed as $(P_1 - P_2)/L$, also denoted as ΔP. The average in-plane flow rate q is given by:

$$q = \frac{e^2}{12\mu}\Delta P \tag{1}$$

where, e is the hydraulic aperture, and μ is the dynamic viscosity of the fluid (10^{-3} Pa · s for water). The solution scheme of the fluid flow calculation is explicit. After a single fluid timestep Δt_f, the fluid volume change over a contact is calculated by summing the change in the flow volume ΔV_C:

$$\Delta V_C = \Delta t_f q \tag{2}$$

The volume change results in an increase in fluid pressure ΔP at the undeforming contact as:

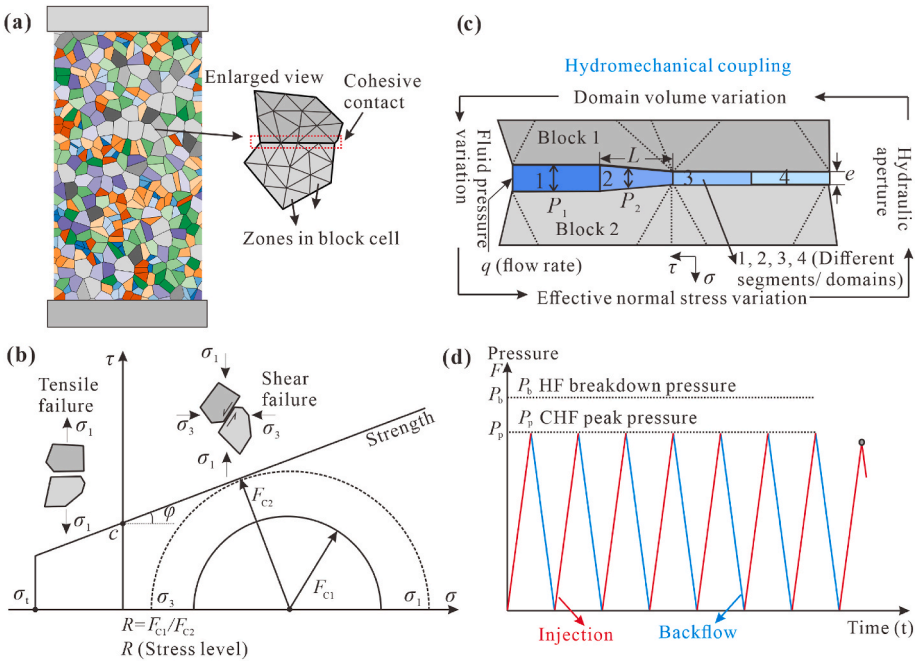

Fig. 1. Schematic showing workflow of simulation accounting for CHF. (a) Block-based discrete element method (DEM) approach. Zoomed-in view illustrates a pair of blocks connected by a cohesive contact. (b) Stress state represented by Mohr circles and failure envelope, where the solid circle indicates the current stress state, and the dashed circle represents the failure stress defined by the Mohr-Coulomb failure envelope. (c) Hydromechanical coupling logic for the DEM model. (d) Cyclic pressure time series for CHF that employs a peak fluid pressure P_p lower than breakdown pressure P_b in HF.

$$\Delta P = K_f(\Delta V_C/V_C) \tag{3}$$

where K_f is the fluid bulk modulus, and V_C is the fluid volume. The fluid exerts this pressure on the surrounding blocks causing deformations that alter the stress states of the contacts. This, in turn, modifies the hydraulic aperture, thereby affecting the flow field (Fig. 1c). When adopting the cubic law for fluid calculation, we assume that the fluid is incompressible and that fluid storage is small in comparison to transmission rates, thus resulting in a steady-state flow.[70] In addition, the blocks are assumed impermeable, a reasonable assumption for the rocks and fracture networks we consider.

2.3. Mechanical fatigue

In conventional HF stimulation, a continuous, monotonic injection is used until the HF breakdown pressure, P_b, is reached (Fig. 1d). It should be noted that the P_b in laboratory scale tests is the fluid pressure that causes fracture formation. However, P_b at underground condition is controlled by pre-existing faults, far-field stress and rock mass strength. CHF employs cyclic high- and low-injection pressures. After an extended CHF treatment, the final fracture occurs at a lower P_b compared to monotonic pressurization for conventional methods. This delayed initiation of fracture at a lower stress level is as a result of subcritical crack growth, where crack growth is influenced by both the level and duration of applied stress. Crack growth velocity, V, can be described using linear elastic fracture mechanics (LEFM)[71] as:

$$V = \alpha_1 e^{\alpha_2(K_I/K_{IC})} \tag{4}$$

where K_I is stress intensity factor for mode I (tensile) loading, K_{IC} is mode I fracture toughness, and α_1 and α_2 are material constants. According to the LEFM model, Potyondy[72] proposed a stress corrosion model to simulate rock fatigue by calculating mesoscale particle bond degradation in DEM. However, in this model, only the tensile stress is considered for quantifying stress to strength ratio R (i.e., $R = F_T/\sigma_t$, where F_T is tensile stress and σ_t is tensile strength). Other empirical fatigue models by Wang and Cai define stress to strength ratio R as F_{C1}/F_{C2} in the compressive regime[73] (Fig. 1b). The Mohr circle with radius F_{C1} represents the stress state of rock, which is calculated as $(\sigma_1+\sigma_3)/2$, and F_{C2} is the radius of Mohr circle at failure state. σ_3 and σ_1 are minimum and maximum principal stresses, respectively. The analytical expression of F_{C2} is given by:

$$F_{C2} = \left[c\cot\varphi + \frac{1}{2}(\sigma_1+\sigma_3)\right]\sin\varphi \tag{5}$$

where c and φ are cohesion and friction angle of the Mohr-Coulomb criterion, respectively.

We define the stress-strength ratio R for both tensile and compressive regimes to calculate fatigue:

$$\begin{aligned} R &= \frac{F_T}{\sigma_t}\ (\text{In tensile regime}) \\ R &= \frac{F_{C1}}{F_{C2}}\ (\text{In compressive regime}) \end{aligned} \tag{6}$$

The relationship between the lifetime (T_L) of rock and stress level R can be derived from laboratory tests,[73,74] considering time- and stress-dependent loading conditions:

$$R(t)^a = 1 - m\ln T_L(t) \tag{7}$$

where a and m are material constants determined by fitting the experimental results, and t is duration of loading. In accordance with tests on granite, parameters a and m are calibrated to be 2 and 0.0124, respectively.[73,75–77] The stress-strength ratio R serves as a critical factor to determine the strength degradation rate.

Evolution of fatigue can be represented by the damage index D:

$$D(t) = 1 - t\Big/e^{\frac{1-R(t)^a}{m}} \tag{8}$$

where D ranges from 1 to 0, representing transit from intact to fully damaged states, respectively.

In the model implementation, we incorporate equation (8) into the DEM model at each incremental timestep Δt as:

$$D(t+\Delta t) = D(t) - \Delta t \Big/ e^{\frac{1-R(t)^a}{m}} \tag{9}$$

Thus, the cohesion and tensile strength of contacts are reduced proportionally to the accumulated damage index D for each response, reflecting the progressive degradation of the material.

2.4. Model calibration

We verify the proposed hydromechanical damage model against experimental results for Pocheon granite reported by Zhuang et al.[25,78] Experiments are on cylindrical granite specimens 50 mm × 100 mm (d × l), with a blind borehole along the center axis. Both HF and CHF experiments are conducted with explicit time integration at a step size of 2 × 10^{-6} s. The average HF P_b is first measured, with water injected into the borehole at a rate of 100 mm^3/s. Then, CHF tests are conducted in new intact specimens with a maximum injection pressure equaling 70 %–100 % of the average HF P_b. A parametric study is then conducted to investigate the influence of material constants by varying a and m at incremental steps of 0.1 and 0.0006, respectively.

We calibrate the DEM model to adjust model parameters until they align with the mechanical behavior observed in laboratory tests. The measured elastic modulus and Brazilian (i.e., indirect) tensile and uniaxial compressive strengths of the Pocheon granite are 58.5 GPa, 8.8 MPa, and 192.1 MPa, respectively[78]; and the best-fit homogeneous-magnitude DEM parameters (Table 1) yield 58.0 GPa, 8.8 MPa and 192.0 MPa, respectively. The DEM simulations show similar fracture patterns in failure compared to laboratory tests (Fig. 2). Thus, we use these calibrated parameters for modeling in this study.

We now simulate HF and CHF on the laboratory scale specimen (Fig. 3a), where the fluid injection is sustained continuously at a rate of 100 mm^3/s, which adheres to laboratory practices. A complete leak-off/backflow test is conducted when reaching P_p at each injection cycle at the same rate. The stress level is controlled by changing CHF P_p magnitudes, which are set to 95 %, 90 %, 85 % and 80 % of the HF P_b, respectively.

To simulate the CHF response at block scale, we utilize a generic 5 m × 5 m model containing randomly generated discrete fractures, with 150 randomly generated discrete fractures, featuring uniformly distributed orientations ranging from −90 ° to 90 ° and lengths uniformly distributed between 0 and 1.6 m, forming a flowing network (DFN) (Fig. 3b and c). The fractures in the DFN serve as planes of weakness and preferred pathways for fluid transport, playing a critical role in driving damage and the evolution in permeability. The initial aperture value of 0.02 mm is assumed for incipient fractures, and a maximum value of 0.1 mm is assumed for the open fractures. A relatively high injection rate of 10 dm^3/s is applied through the central injection point of the model, and a step size of 2 × 10^{-6} s is chosen to ensure model stability. We examine two stress ratios (K) of 1.17 and 1.40, where the horizontal stress σ_H is set to 35 MPa, and the vertical stress σ_V is set to 30 MPa and 25 MPa, respectively. To qualitatively analyze the CHF for block scale application, we adopt the calibrated parameters of the Pocheon granite reduced by 10 % to represent the strength reduction due to natural planes of weakness.

Table 1
Calibrated parameters used in the numerical modeling.

	Parameters representing contacts	Value
σ_t	Tensile strength (MPa)	8.36
c	Cohesive strength (MPa)	89
k_T	Tangential stiffness (N/m)	1.8 × 10^{14}
k_N	Normal stiffness (N/m)	1.8 × 10^{14}
φ_j	Friction angle at contact (°)	20
μ	Fluid dynamic viscosity	1.01 × 10^{-3}
β	Damping coefficient	0.5
	Parameters used in blocks	
ρ	Block density kg/m^3	2609
K	Bulk modulus (GPa)	61

In the simulation, contact breakage is characterized by tensile, shear, and mixed-mode failures. We also investigate the shear reactivation of existing fractures. To capture the resulting seismicity, particle velocity in the y-direction (y-velocity) is recorded at a monitoring location 2 m above the injection point, with absorbing boundaries applied to the model to dampen reflected waveforms. Particle y-velocity is recorded continuously for each explicit numerical step, equivalent to a data acquisition frequency of 500 kHz. To mitigate the influence of the numerical noise and deformation of blocks under changing stress conditions, the continuous recording is filtered with a band-pass filter spanning the range 50–450 kHz. Then, seismic events and the corresponding waveforms are identified by a y-velocity amplitude threshold of 0.001 m/s. The spectra of waveforms are computed by Fast Fourier Transform (FFT), and then normalized to [0, 0.5] Hz according to a Nyquist frequency of 250 kHz.[79] Finally, we analyze the evolution of failure mechanisms during HF and CHF stimulations by comparing failure types and the amplitude-frequency spectra.

For the HF injection, the simulation is stopped after breakdown but before the hydraulic fracture reaches the boundary of the model. For comparison, the CHF simulations are stopped with the same cumulative volume of injection to the corresponding HF. The equivalent permeability is measured after the stimulation by applying constant hydraulic pressure boundaries on adjacent faces of the model.[80] After the CHF injections, pressures are allowed to completely dissipate before permeability is measured across the stimulated zones (Fig. 7 c&d) by applying a fluid pressure differential of 10 MPa in the two orthogonal directions. Once a stable flow rate is achieved, permeability is calculated using Darcy's law as:

$$k = \frac{\mu Q L_b}{\Delta P A} \tag{10}$$

where k is the permeability (m^2); Q is the flow volume per second; L_b is the flow length between the two flow boundaries; $\mu = 10^{-3}$ Pa · s is liquid dynamic viscosity; ΔP is the pressure difference across the flow path; and A is cross sectional area (assuming unit thickness).

3. Results

We complete modeling on laboratory scale samples (3.1 & 3.2) and extend it to block scale experiments (3.3 & 3.4). The laboratory scale experiments examine, in detail, the influence of two different stresses and then match model results with a broad array of experiments. The block scale simulations explore the impact of stress obliquities of 1.17 and 1.40 on mechanistic and hydraulic response.

3.1. Laboratory scale simulation results

The calibrated laboratory scale model simulation returns a hydraulic fracturing breakdown pressure (i.e., HF P_b) of 6.93 MPa (Fig. 4a), closely matching the laboratory test result of 6.90 MPa.[25] Before reaching HF P_b, a total fluid volume of 35.34 mm^3 is injected. When the contacts on the borehole wall break, additional fracture volume becomes available for fluid flow, resulting in a noticeable drop in the fluid pressure (Fig. 4a). The macroscale fracture and stress distribution observed after reaching the HF P_b are also depicted in Fig. 4a, revealing the formation of a primary fracture without complex branching.

3.2. CHF laboratory simulations under different stress levels

We present two simulation results in detail to show the anticipated evolution of fluid pressure, damage index value and local stress surrounding the borehole (Fig. 4b–c) for laboratory scale samples. During the CHF test employing P_p at 95 % of HF P_b, failure occurs on the fourth

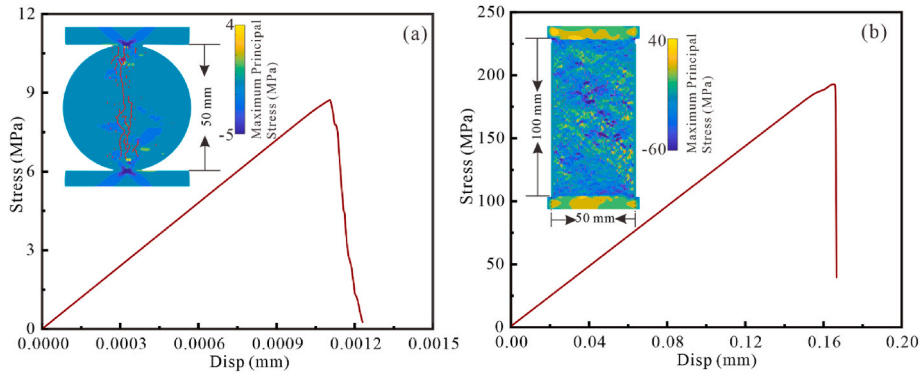

Fig. 2. Calibration results include numerical tensile and compressive strength tests. (a) Stress-displacement curve and the failure fracture pattern of the numerical Brazilian tensile strength test. (b) Stress-displacement curve and the failure fracture pattern of the numerical uniaxial compressive strength tests. Lines populating sample sections represent evolving fracture network from local rupture.

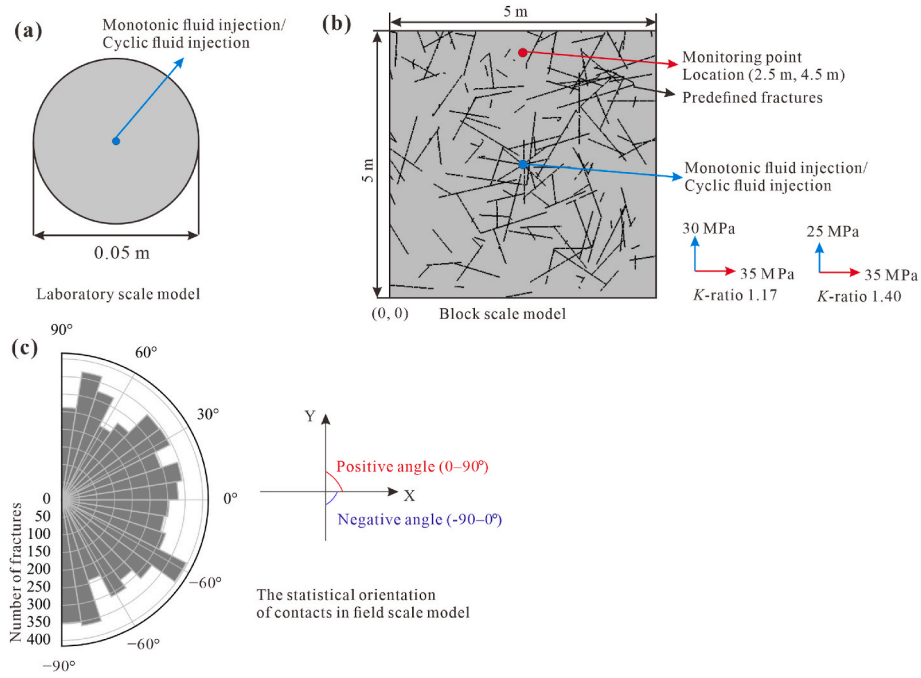

Fig. 3. Geometries of numerical models used for HF and CHF modeling. (a) Laboratory scale model. (b) Block scale model incorporates pre-defined discrete fracture network (DFN) and two far-field stress obliquities (*K*-ratios). (c) Resulting orientation distribution of block contacts in block scale model with azimuth.

injection cycle, relative to the third cycle in the laboratory. At a lower injection pressure at 80 % of HF P_b, the number of cycles increases to 30 (Fig. 4c), whereas laboratory result shows 46 cycles.[25]

Hydromechanical fatigue affects the strength of contacts impacted by fluid pressures (Fig. 4). For a specific contact (e.g., zoomed-in views in Fig. 4), the fatigue rate, represented by the slope of the red curves, is highest at P_p. Under a stress level of 95 % HF P_b, the damage index decreases by 0.0140 with each injection cycle, while under 80 % HF P_b, it decreases by 0.0074 after every injection cycle. The final damage index values at breakdown are 0.95 and 0.7814 for 95 % and 80 % HF P_b, respectively. Thus, employing a lower stress level increases the lifetime of the rock and reduces the final damage index at the failure point, resulting in a lower CHF P_b. After the CHF P_b, a pair of fractures form and propagate in opposite directions. The injected fluid volumes when breakdown is reached are 28.88 mm^3 and 33.96 mm^3 for 80 % and 95 % HF P_b, respectively, reducing the required fluid volume by 18.3 % and 3.9 % compared to HF, respectively.

In laboratory tests, the number of injection cycles varies widely even under the same stress level, due to the heterogeneous strength of natural rock samples.[25] This heterogeneity can be reproduced by varying parameters a and m in Equation (7) as demonstrated in the parametric study (Fig. 5). Although the laboratory results are scattered, the models effectively capture the general trend, with a and m being positively and negatively related to the lifetime of the rock, respectively. This validation confirms the effectiveness of the newly developed hydromechanical damage model.

3.3. Low stress ratio block response (35 MPa σ_H: 30 MPa σ_V)

We first conduct the block scale simulation at a *K*-ratio of 1.17, with a horizontal stress of 35 MPa and a vertical stress of 30 MPa. Through continuous injection, the reservoir reaches its HF P_b at 37.2 MPa (Fig. 6a).

The CHF stimulation is completed under 94 % of HF P_b (35 MPa) and stopped at the 8th injection cycle. Injection-induced seismic events primarily occur during the injection phase of each cycle (blue points in Fig. 6a). A total of 13 seismic events for HF and 104 for CHF (Fig. 6a–c) are identified from the continuous seismic signals, which may be linked

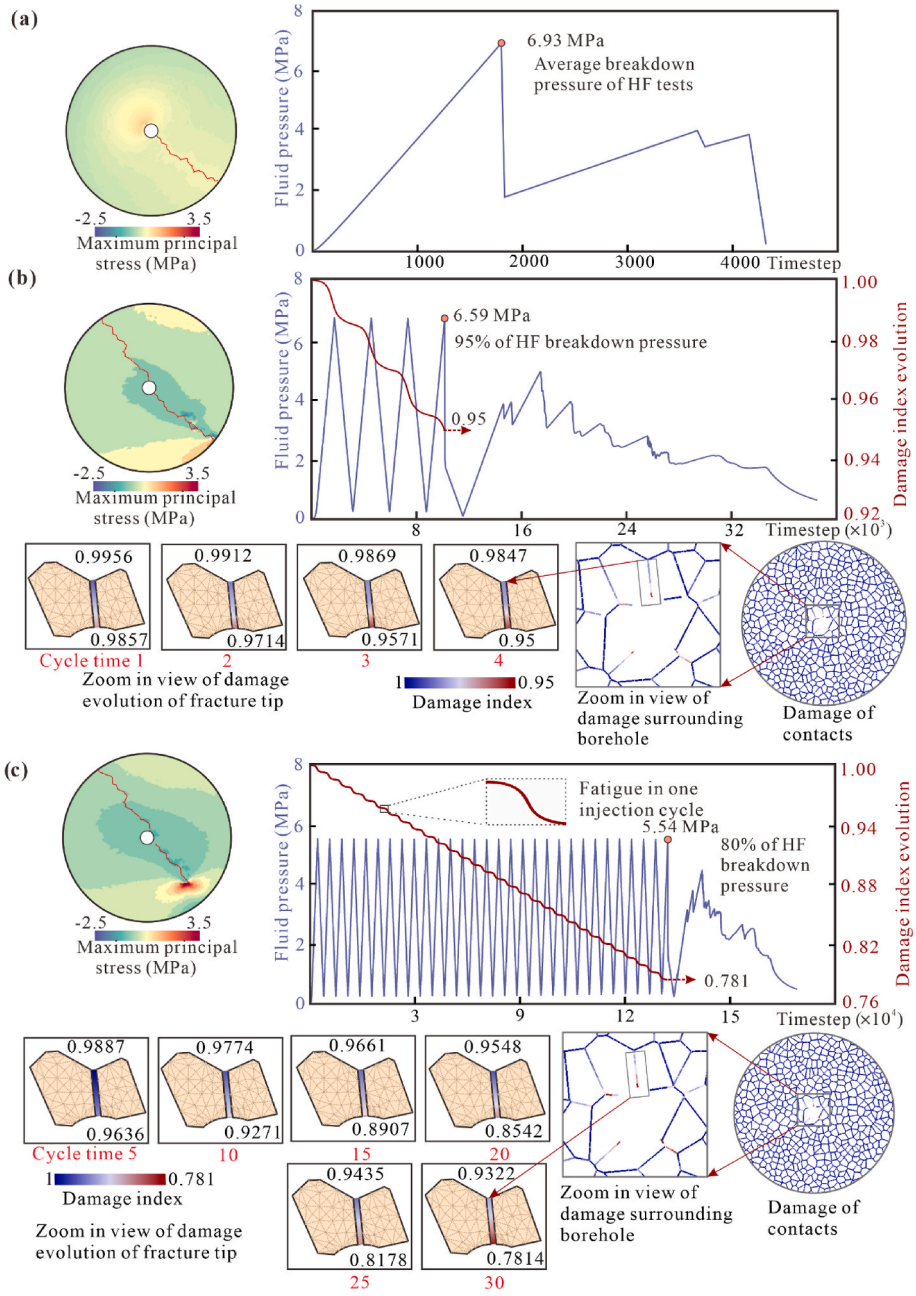

Fig. 4. Numerical results for laboratory scale HF and CHF tests. (a) Stress contour map of HF stimulation captured above P_b. Fluid pressure recorded at the center of the borehole establishes P_b as a reference for the CHF tests. (b) Results of the CHF test conducted at 95 % of the HF P_b. (c) Results of the CHF test conducted at 80 % of HF P_b. Blue curve illustrates the variation in fluid pressure at the borehole, and the red curve depicts the contact damage evolution near injection location. Lower parts of (b) and (c) represent zoomed-in view of damage evolution of contacts over different injection cycles of CHF. (For interpretation of the references to color in this figure legend, the reader is referred to the Web version of this article.)

to the failure of intact cohesive contacts or the shear reactivation of existing fractures. In the HF test, the peak particle velocity in the y-direction (PPV-y) reaches 0.32 m/s, while in CHF tests, it only reaches 0.22 m/s, representing a 31 % reduction (Fig. 6b). The PPV-y and dominant frequency of seismic waves show variations according to the injection pressure, in general, the higher the fluid pressure, the higher the PPV-y, and the mainshock in each injection cycle occurs at each peak pressure. High PPV-y events are associated with low dominant frequency as illustrated by the spectrum (Fig. 6c and d).

Significant new fracturing occurs mainly during CHF1–3 and CHF7–8, with no new fractures during CHF5–6 (Fig. 6e). The first injection cycle of the CHF (CHF1) shows similar patterns to HF: the first seismic event appears at a fluid pressure of 16.7 MPa, and all the seismic events during CHF1 and HF injections are associated with formation of new fractures. During CHF2–8, most seismic events are shear reactivation events, and there is no noticeable increase in new fractures before the fluid pressure reaches 33.5 MPa.

We then compare the dominant frequency, wave amplitude, and corresponding fluid pressure of seismic events (Fig. 6f). Notably, after the initial injection cycle, injection-induced shear reactivations occur progressively earlier (i.e., at a lower fluid pressure) than in the previous cycles (Fig. 6 a&f). The dominant frequency of these shear reactivation seismic events fluctuates with no obvious trend; however, the mainshock consistently presents a low dominant frequency. The PPV-y of the mainshocks show a systematic increase from the first CHF cycle to the fourth cycle (CHF4) and then decrease until the end of the stimulation.

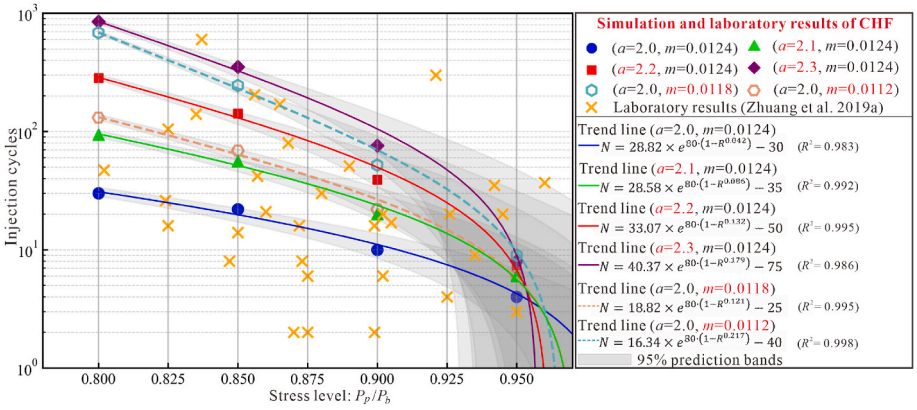

Fig. 5. Number of injection cycles required to reach overall failure during CHF stimulation under varying stress levels. The results include a comparison between laboratory observed data and numerical simulations using different material constants *a* and *m* used in Equation (7).

After the largest mainshock event in CHF4, the number of shear reactivation events in each CHF cycle approximately doubled. The wave PPV-y of mainshocks in CHF are all smaller than the mainshock in the HF.

The stress disturbance near the borehole is significantly affected by the fracture network and fluid pressure. After CHF, multiple high stress concentration zones can be observed in the vicinity of the borehole, which are not seen in the HF (Fig. 7a–b). Fractures propagate, in general, perpendicular to the minimum principal stress, but are highly influenced by the discrete fracture network (DFN). After CHF stimulation, a more complex fracture network is formed than for HF, with more pre-existing fractures connected, and the fractures also develop more extensively in the vertical direction. Highly stressed zones develop around fracture tips and in the rock mass bounded by fractures.

The horizontal permeability measured in HF and CHF tests is 1.58×10^{-10} m^2 and 1.14×10^{-9} m^2, respectively (Fig. 7c and d). Similarly, the vertical permeability for HF and CHF tests is 2.49×10^{-10} m^2 and 1.65×10^{-9} m^2, respectively (Fig. 8c–d). CHF stimulation under the current far-field stress conditions can enhance permeability in horizontal and vertical directions by factors of 6.21 and 5.63 compared to HF, respectively.

3.4. High stress ratio response (35 MPa σ_H:25 MPa σ_V)

For comparison, we conduct another block scale modeling under 35 MPa σ_H and 25 MPa σ_V, representing an increased stress ratio for a *K*-ratio of 1.40. During the HF continuous injection, the HF P_b is 30.8 MPa (Fig. 8a), lower than previous modeling at 37.2 MPa. The CHF stimulation is performed under 94 % HF P_b (29 MPa) and stopped at the 6th injection cycle. A total of 8 and 56 seismic events are identified in HF and CHF (Fig. 8b–c), respectively. Under HF stimulation, the PPV-y of seismic wave is 0.28 m/s, which is reduced by 25 % to 0.21 m/s in the CHF test.

The seismic events show similar temporal and waveform patterns to the previous lower stress ratio case. The dominant frequency and PPV-y of seismic waves show negative and positive correlations with the fluid pressure, respectively, and the mainshock of each injection cycle occurs near the peak fluid pressure (Fig. 8 c&d).

The formation of new fractures primarily occurs during CHF1–4 and CHF6, with no new fractures observed during CHF5 (Fig. 8e). For both CHF1 and HF, the first new fracture appears at 16.5 MPa and subsequent seismic events are accompanied by new fractures. During CHF2–6, new fractures are generated when fluid pressure is above 27.6 MPa and near the peak pressure of 29.0 MPa.

The wave PPV-y of mainshocks systematically increases from the first CHF cycle to the third, then decreases toward the end of stimulation. Notably, all mainshocks in CHF exhibit smaller PPV-y compared to the mainshock in HF (Fig. 8f). The initial shear reactivation at each injection cycle occurs progressively earlier. After CHF3, some shear reactivation induced seismic events show relatively high PPV-y values, and the number of shear activation events is approximately doubled. In addition, previous CHF modeling with a *K*-ratio of 1.17 generates 496 fractures, comprising 81 (16.36 %) shear, 76 (15.35 %) tensile, and 338 (68.29 %) mixed-mode fractures. At a *K*-ratio of 1.40, CHF produces 548 fractures, with 208 (37.96 %) shear, 63 (11.50 %) tensile, and 277 (50.54 %) mixed-mode fractures. Thus, as the *K*-ratio increases, the percentage of shear fractures rises by 21.6 %, while tensile and mixed-mode fractures decrease by 3.85 % and 17.73 %, respectively.

For this high stress ratio case (vertical in-situ stress decreases from 30 MPa to 25 MPa), the HF P_b reduces from 37.2 MPa to 30.8 MPa. Six CHF injection cycles are needed to reach the same volume of injection as the HF. HF and CHF induced fractures predominantly develop in the horizontal direction (Fig. 9), and both show more extensive development than in the previous case with a smaller *K*-ratio. The fractures in CHF develop into a more complex network than in HF, and highly stressed areas are observed at the fracture tips and in regions constrained by fractures. In addition, due to the extensively developed fractures in the horizontal direction, the stress concentration influences the growth of adjacent fractures (Fig. 9b), i.e., a stress shadow effect, where extensive compaction can reduce the permeability of such fractures.

Permeability tests reveal that the horizontal permeability for HF and CHF stimulations is 6.11×10^{-10} m^2 and 8.96×10^{-9} m^2, respectively (Fig. 9c). The vertical permeability for HF and CHF tests is 6.01×10^{-11} m^2 and 1.03×10^{-9} m^2, respectively (Fig. 9d). Thus, CHF under this in-situ stress condition increases horizontal permeability by 13.67 times and vertical permeability by 16.14 times. Notably, despite the overall increase in horizontal permeability with CHF, one fracture located in the stress shadow exhibits a lower flow rate compared to the HF test (Fig. 9 c&d).

An increase in the *K*-ratio from 1.17 to 1.40 leads to a 2.87-fold rise in horizontal permeability in HF and a 6.86-fold rise in CHF, while vertical permeability decreases by 40.43 times in HF and 0.6 times in CHF. These trends are driven by changes in fracture orientations (Fig. 10): horizontal fractures increase by 27 (14.7 %) in HF and 68 (27.9 %) in CHF, whereas vertical fractures decrease by 21 (47.3 %) in HF and 67 (58.77 %) in CHF.

4. Discussion

4.1. Key mechanisms controlling outcomes of CHF

The key role of fatigue damage during CHF as a principal mechanism controlling seismicity has long remained unclear since it was first

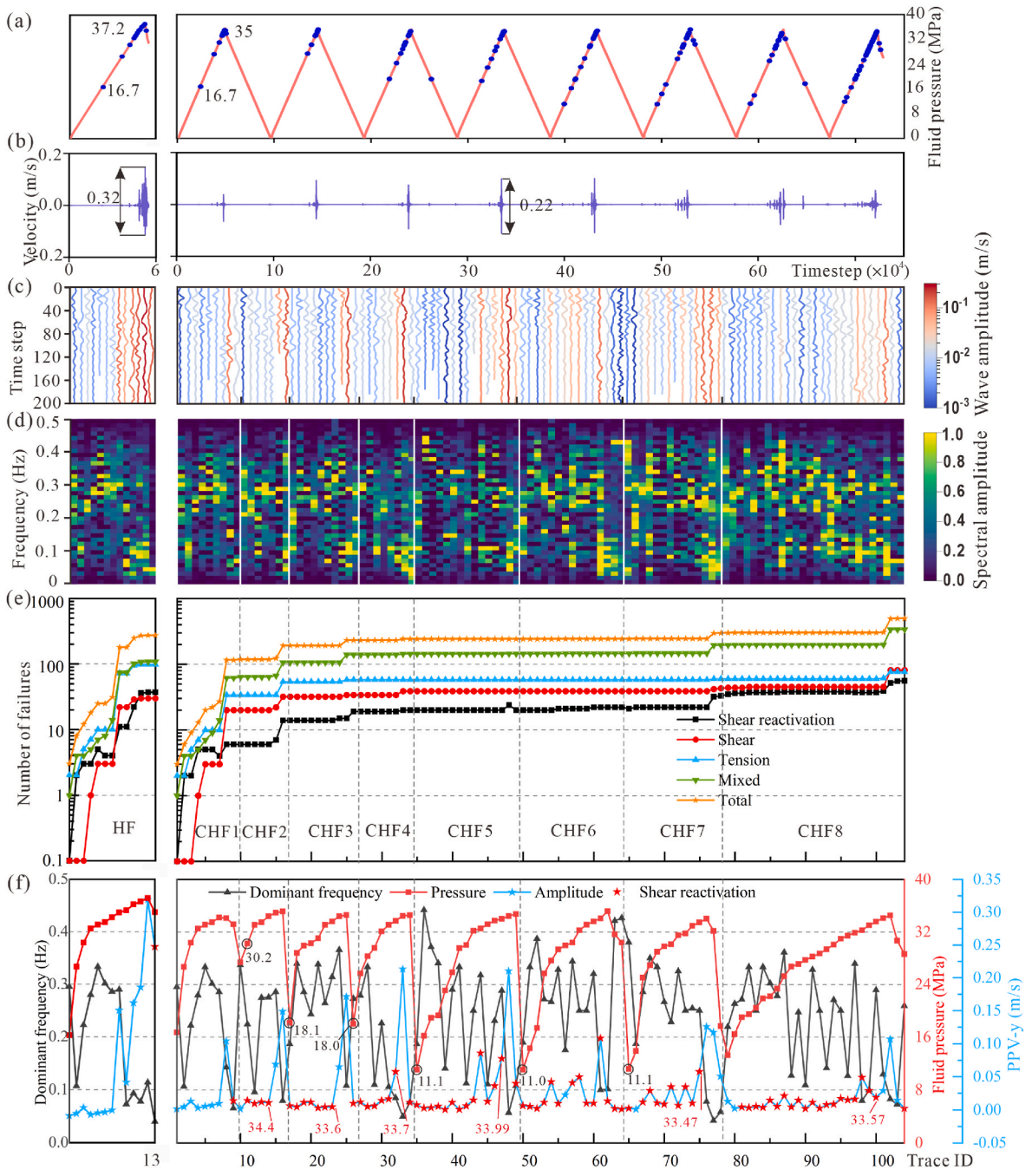

Fig. 6. Response for constant (left panels; HF) and cycled (right panels; CHF) pressures during block scale stimulation for the *K*-ratio 1.17. (a) Applied fluid pressure schedule. (b) Continuous seismic waves recorded from observation point 2 m from the borehole. (c) Seismic waveforms recorded during HF and CHF stimulations with color representing wave amplitude and corresponding wave spectrograms illustrated in (d). (e) Number of contact failures by mode. (f) Comparison of dominant frequency, PPV-y, and fluid pressure for each seismic event, with pure shear reactivation events highlighted by red stars and first shear reactivation event at each cycle highlighted by black circles. (For interpretation of the references to color in this figure legend, the reader is referred to the Web version of this article.)

proposed. However, we successfully demonstrate a key role of hydro-mechanical fatigue congruent with the CHF laboratory calibration tests. This is achieved by incorporating the newly developed damage model with sub-critical crack growth under hydromechanical coupled conditions as a key component. This both verifies our model and suggests a key mechanistic control in the observed outcomes of CHF.

Early tests by Zang et al. suggested that CHF produces a narrower zone of tensile and shear fractures.[15] They argued that continuous injection prevents the fracture from optimizing its growth path, whereas CHF allows sufficient time for adaptation, resulting in a narrower damage zone. In contrast, Zhuang et al. compared creep and cyclic hydraulic fracturing and proposed that two key fatigue mechanisms—infiltration and subcritical crack growth—contribute to rock damage.[25] Their X-ray computed tomography results indicated that CHF induces more small fracture branches compared to HF, attributing this to the longer injection duration, which increases infiltration and alters fracture initiation and propagation due to structural heterogeneity.

Our findings suggest that CHF does not significantly alter fracture patterns in laboratory scale intact rock, which is typically assumed to be impermeable. Fatigue effects are localized near the borehole and do not cause widespread damage. The number of CHF injection cycles can vary significantly due to strength heterogeneity of samples, which can be

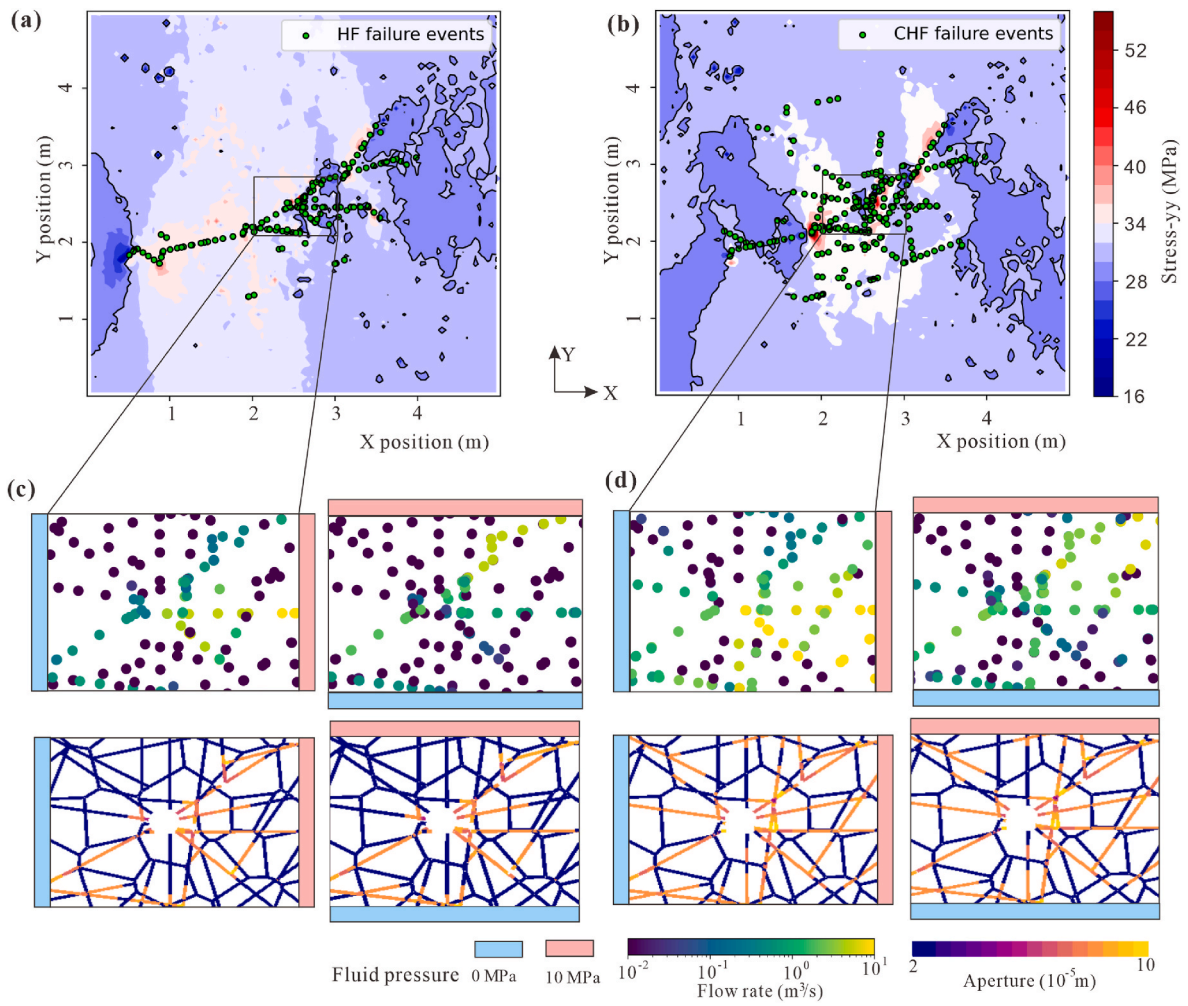

Fig. 7. Comparison of failure states for HF (left) and CHF (right) for a *K*-ratio 1.17. (a) and (b) show stress contour maps and the new fractures (green dots) resulted from HF and CHF, respectively. (c) and (d) present the results of numerical permeability tests performed post-failure, with fluid pressures of 0 and 10 MPa applied on facing boundaries alternately in X- and Y-directions. The colored dots represent grid points separating sub-domains as shown in Fig. 1c, where fluid flux is calculated. The lower parts of (c–d) show the fracture aperture comparisons between HF and CHF stimulations. (For interpretation of the references to color in this figure legend, the reader is referred to the Web version of this article.)

simulated by modifying the material constants a and m in Equation (7). However, at large scales, natural rock masses with pre-existing fractures enable fluid infiltration, leading to more extensive fatigue effects and a more complex fracture network.

Early studies on cyclic loading in rock primarily focused on purely mechanical fatigue behaviors (e.g., Wang & Cai[73]). While mechanical fatigue can be explained by subcritical crack growth theories, such as linear elastic fracture mechanics (LEFM) or by the decohesion and loosening of mineral bonds,[81] hydromechanical fatigue involves additional complexities. For instance, the stress shadow effect – increased stress in the region surrounding fractures – may inhibit further fracture initiation and propagation, resulting in shorter and narrower fractures. Fractures within the stress shadow experience closure stresses exceeding the original in-situ stress, requiring higher pressure for propagation.[82]

Additionally, cyclic tensile fatigue emerges as the dominant mechanism in unconfined CHF tests. However, in confined rock masses at depth, the mechanism of fatigue failure becomes more complex. This complexity arises from the shear reactivation of pre-existing fractures following their initial injection-induced opening within the DFN.

With this new hydromechanical fatigue model, we simulate CHF both in laboratory and block scale conditions. The simulations of laboratory cases show significant reduction in breakdown pressure, which coincides with previous experimental investigations on different types of rocks.[25–27] The outcomes of CHF in block scale simulations also show agreement with Zimmermann in permeability improvement.[3]

4.2. Induced seismicity during HF and CHF

Seismicity induced by HF and CHF stimulations arises from the shear reactivation of pre-existing faults or the creation of new fractures.[83–85] By analyzing fracture statistics and spectral data, we observe that shear reactivation events at the peak injection pressure tend to generate high-amplitude, low-frequency seismic waveforms. For instance, during CHF4-6 at a *K*-ratio of 1.17 and CHF5 at a *K*-ratio of 1.40, no new fractures are formed, but high-amplitude mainshocks are detected (Figs. 6 and 8). This supports the interpretations that perceptible seismicity primarily results from the shear reactivation of fractures.[84]

Seismic events exhibit distinct characteristics under HF and CHF stimulations. Pure shear reactivation induced seismicity is dominant in CHF from the second injection cycle onward but is not observed in HF. The formation of new fractures is typically accompanied by shear reactivation, except during CHF5–6 (*K*-ratio = 1.17) and CHF5 (*K*-ratio = 1.40), where no new fractures form. This occurs because fluid preferentially infiltrates existing fractures, and the available energy is insufficient to initiate new fractures. Nevertheless, CHF-induced fatigue damage progressively weakens the rock, reducing the pressure required

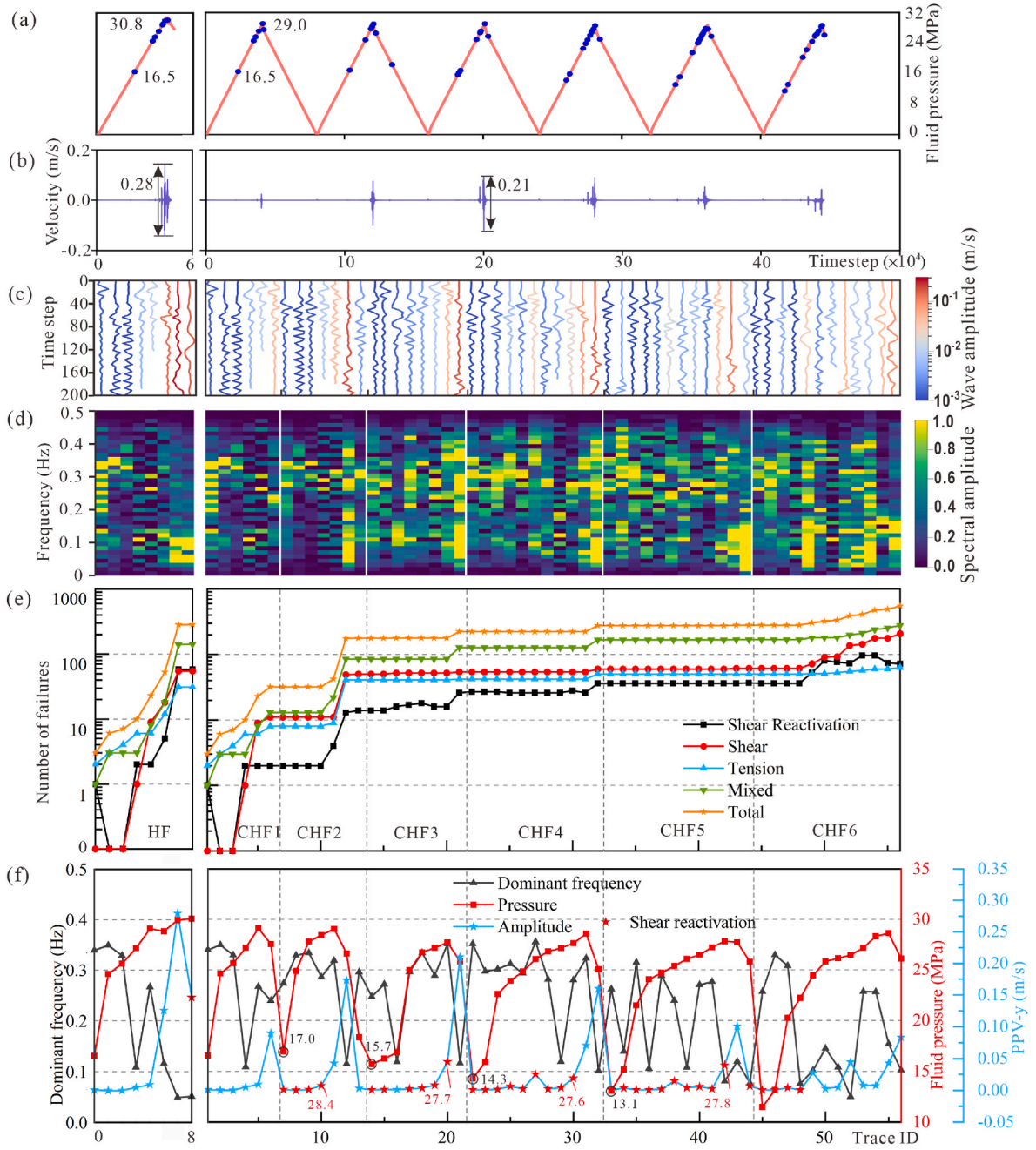

Fig. 8. Response for constant (left panels; HF) and cycled (right panels; CHF) pressures during block scale stimulation for the *K*-ratio 1.40. (a) Applied fluid pressure schedule. (b) Continuous seismic waves recorded from observation point 2 m from the borehole. (c) Seismic waveforms recorded during HF and CHF stimulations with color representing wave amplitude and corresponding wave spectrograms illustrated in (d). (e) Number of contact failures by mode. (f) Comparison of dominant frequency, PPV-y, and fluid pressure for each seismic event, with pure shear reactivation events highlighted by red stars and first shear reactivation event at each cycle highlighted by black circles. (For interpretation of the references to color in this figure legend, the reader is referred to the Web version of this article.)

for subsequent fracture propagation, reducing shear resistance and promoting earlier shear reactivation with successive injection cycles.

Under CHF, the generation of new fractures and the connection of pre-existing fractures is a gradual process, with energy dissipated over time through fatigue damage and shear reactivation. The magnitude of CHF induced seismicity increases initially, peaks, and then declines over successive cycles, while the number of shear reactivations approximately doubles after the largest magnitude event. This indicates that stress redistribution within the rock mass occurs through frequent shear reactivations, which release strain energy, at an elevated rate but on small fractures, without producing large-magnitude events as in HF. This highlights the potential of CHF to mitigate induced seismic hazards.

The influence of the stress ratio (*K*-ratio) on induced seismicity is comparable in both CHF and HF. Fractures are more prone to shear failure under a high *K*-ratio, which results in a lower overall magnitude of seismic events compared to a lower *K*-ratio condition.

4.3. *Permeability evolution during CHF*

Enhancing permeability is essential for efficient subsurface energy extraction and for increasing the injectivity and storage capacity of geological carbon sequestration. Our findings demonstrate that CHF significantly outperforms HF in generating new fractures and results in larger number of induced seismic events at smaller magnitudes. Under a

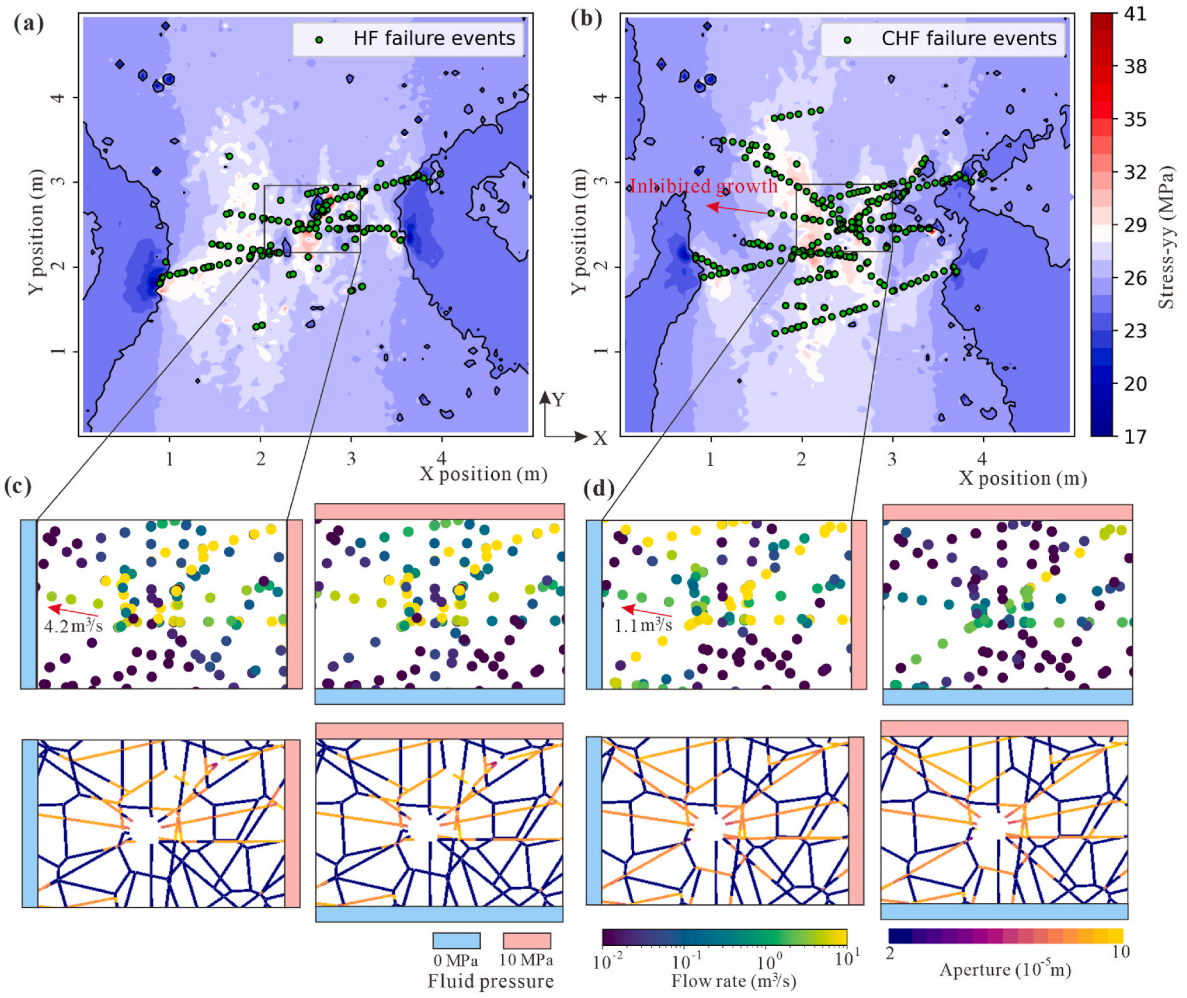

Fig. 9. Comparison of failure states for HF (left) and CHF (right) for a *K*-ratio 1.40. (a) and (b) show stress contour maps and the new fractures (green dots) resulted from HF and CHF, respectively. (c) and (d) present the results of numerical permeability tests performed post-failure, with fluid pressures of 0 and 10 MPa applied on facing boundaries alternately in X- and Y-directions. The colored dots represent grid points separating sub-domains as shown in Fig. 1c, where fluid flux is calculated. The lower parts of (c–d) show the fracture aperture comparisons between HF and CHF stimulations. (For interpretation of the references to color in this figure legend, the reader is referred to the Web version of this article.)

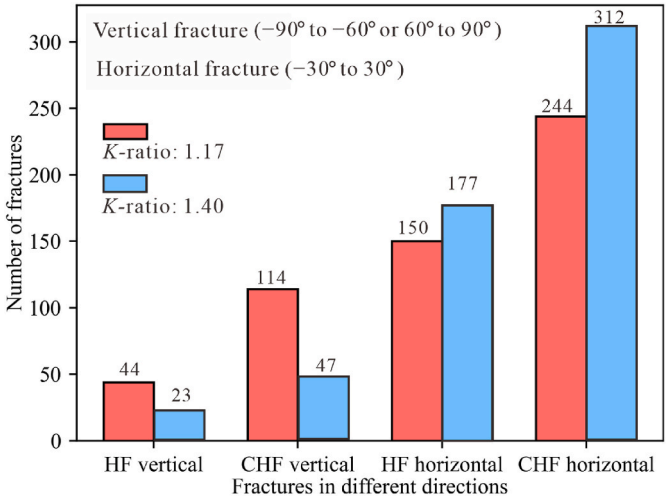

Fig. 10. Effect of in-situ stress on fracture orientations: Comparison of vertical and horizontal fracture counts for different *K*-ratios.

K-ratio of 1.17, CHF produces 93 % more fractures and 700 % more microseismic events than HF, while at a *K*-ratio of 1.40, CHF generates 81 % more fractures and 600 % more microseismic events. This enhanced fracture network development increases rock mass permeability, supporting observations from laboratory and field studies.[27,30,31]

However, CHF can also reduce permeability in certain cases. For example, Zang et al. and Niemz et al. reported that incrementally increasing P_p during CHF may produce a more persistent but narrower fracture network compared to HF, potentially lowering permeability near the borehole due to fewer open fractures.[15,20] Changes in the local stress field[86,87] can further influence fracture behavior, either enhancing or reducing permeability. In our case study with a *K*-ratio of 1.17 (Fig. 9), we observe that a fracture within the stress shadow exhibits restrained growth and lower permeability in CHF compared to HF. The stress shadow effect from multiple adjacent faults in CHF alters the stress field around each fracture, potentially reducing rock mass permeability and influencing the efficiency of CHF treatments.

To optimize CHF design for mitigating induced seismicity and enhancing permeability, numerical models could be further developed. Future studies could explore cyclic injection schemes with progressively increasing flow rates, as suggested by Hofmann et al.[19] The 2D simulations simplify fracture planes, which neglects the clogging and dilation effect for real fracture planes, and it may increase the equivalent

permeability. For instance, Vogler et al.[88] found that cyclic loading can reduce permeability by one order of magnitude due to wear products clogging fluid flow paths, which should be considered in future modeling. For the block-based DEM simulation framework, the aperture of fractures is dependent on the stiffness of fracture plane, hydromechanical stress state, and pre-defined residual and maximum aperture values. Although we provide a fair comparison between HF and CHF in the aspect of permeability improvement, the influence of above-mentioned factors on permeability variation is not considered in this study. Additionally, fluid chemical corrosion which weakens rock strength and induces long-term fatigue,[89,90] could be incorporated into governing equations. Lastly, this study focuses on a homogeneous and isotropic rock mass and relatively permeable DFNs. Future research should address the uncertainty in rocks that exhibit strong anisotropy and lower permeability (i.e., shale) to improve the applicability of the results.

5. Conclusion

A new time- and stress-dependent hydromechanical damage model is developed to simulate fatigue damage in CHF. The model successfully captures the role of fatigue damage in the evolution fracture propagation, fluid flow and the triggering of induced seismicity. At the laboratory scale, fatigue damage is primarily driven by cyclic tensile failure. However, at the block scale, the fatigue process becomes more complex due to the shear reactivation of fractures under in-situ stress conditions. In block scale modeling, the magnitude of mainshocks systematically increases from the first CHF pressurization cycle to the peak cycle, followed by a gradual decrease until the end of the stimulation. In CHF, shear reactivation serves as the dominant mode of seismic reactivation, starting from the initial injection-induced opening of the DFN, whereas in HF, seismicity primarily arises from the formation of new fractures. With progressive CHF fatigue, shear reactivation occurs earlier and at lower fluid pressures. This process dissipates energy through multiple small events and results in a lower mainshock magnitude in CHF compared to HF. The permeability of the rock mass after CHF is higher than after HF due to the development of a more extensive and penetrative fracture network. A reduction in vertical stress decreases the number of fractures generated in the vertical direction while increasing horizontal fractures, leading to corresponding changes in permeability. Stress shadows caused by intensive compaction near faults can inhibit the propagation of adjacent fractures and reduce permeability. Additionally, a higher *K*-ratio results in a greater proportion of shear fractures and a smaller proportion of tensile fractures. This study elucidates the mechanisms governing failure evolution and induced seismicity during CHF, providing valuable insights for field applications aimed at mitigating injection-induced earthquakes and improving permeability.

CRediT authorship contribution statement

Chang Xia: Writing – review & editing, Writing – original draft, Visualization, Validation, Methodology, Investigation, Formal analysis, Data curation, Conceptualization. **Huanyu Wu:** Software, Methodology. **Ki-Bok Min:** Writing – review & editing, Methodology, Investigation, Conceptualization. **Derek Elsworth:** Writing – review & editing, Supervision, Investigation, Conceptualization. **Qi Zhao:** Writing – review & editing, Writing – original draft, Visualization, Validation, Supervision, Software, Resources, Project administration, Methodology, Investigation, Funding acquisition, Formal analysis, Data curation, Conceptualization.

Declaration of competing interest

The authors declare that they have no known competing financial interests or personal relationships that could have appeared to influence the work reported in this paper.

Acknowledgments

We thank the anonymous reviewers for their insightful comments and suggestions. This work is supported by the Early Career Scheme and the General Research Fund of the Research Grants Council of the Hong Kong SAR, China (Project No. PolyU 25220021, PolyU 15227222, and PolyU 15229723) and the PolyU FCE Young Researcher Collaborative Research Fund (P0056408). D. Elsworth gratefully acknowledges support from the G. Albert Shoemaker endowment.

Data availability

Data will be made available on request.

References

1. Hubbert MK, Willis DG. Mechanics of hydraulic fracturing. *Transac AIME*. 1957;210 (1):153–168. https://doi.org/10.2118/686-G.
2. Haimson B, Fairhurst C. Hydraulic fracturing in porous-permeable materials. *J Petrol Technol*. 1969;21(7):811–817. https://doi.org/10.2118/2354-PA.
3. Zimmermann G, et al. Permeability enhancement and fracture development of hydraulic in situ experiments in the aspo hard rock laboratory, Sweden. *Rock Mech Rock Eng*. 2019;52(2):495–515. https://doi.org/10.1007/s00603-018-1499-9.
4. Brown DW, et al. *Mining the Earth's Heat: Hot Dry Rock Geothermal Energy*. Berlin: Springer; 2012.
5. Boschi C, et al. Enhanced CO2-mineral sequestration by cyclic hydraulic fracturing and Si-rich fluid infiltration into serpentinites at Malentrata (Tuscany, Italy). *Chem Geol*. 2009;265(1-2):209–226. https://doi.org/10.1016/j.chemgeo.2009.03.016.
6. Legarth B, Huenges E, Zimmermann G. Hydraulic fracturing in a sedimentary geothermal reservoir: results and implications. *Int J Rock Mech Min Sci*. 2005;42(7-8):1028–1041. https://doi.org/10.1016/j.ijrmms.2005.05.014.
7. Grigoli F, et al. Current challenges in monitoring, discrimination, and management of induced seismicity related to underground industrial activities: a European perspective. *Rev Geophys*. 2017;55(2):310–340. https://doi.org/10.1002/2016rg000542.
8. Guglielmi Y, et al. Seismicity triggered by fluid injection-induced aseismic slip. *Science*. 2015;348(6240):1224–1226. https://doi.org/10.1126/science.aab0476.
9. Schultz R, Beroza GC, Ellsworth WL. A risk-based approach for managing hydraulic fracturing-induced seismicity. *Science*. 2021;372(6541):504. https://doi.org/10.1126/science.abg5451.
10. Ellsworth WL. Injection-induced earthquakes. *Science*. 2013;341(6142):142. https://doi.org/10.1126/science.1225942.
11. Schultz R, et al. Hydraulic fracturing-induced seismicity. *Rev Geophys*. 2020;58(3), e2019RG000695. https://doi.org/10.1029/2019RG000695.
12. Häring MO, et al. Characterisation of the Basel 1 enhanced geothermal system. *Geothermics*. 2008;37(5):469–495. https://doi.org/10.1016/j.geothermics.2008.06.002.
13. Grigoli F, et al. The November 2017 M w 5.5 Pohang earthquake: a possible case of induced seismicity in South Korea. *Science*. 2018;360(6392):1003–1006. https://doi.org/10.1126/science.aat2010.
14. Majer EL, et al. Induced seismicity associated with enhanced geothermal systems. *Geothermics*. 2007;36(3):185–222. https://doi.org/10.1016/j.geothermics.2007.03.003.
15. Zang A, et al. Fatigue hydraulic fracturing by cyclic reservoir treatment enhances permeability and reduces induced seismicity. *Geophys J Int*. 2013;195(2):1282–1287. https://doi.org/10.1093/gji/ggt301.
16. Zang A, et al. How to reduce fluid-injection-induced seismicity. *Rock Mech Rock Eng*. 2019;52(2):475–493. https://doi.org/10.1007/s00603-018-1467-4.
17. Hofmann H, et al. Cyclic soft stimulation (CSS): a new fluid injection protocol and traffic light system to mitigate seismic risks of hydraulic stimulation treatments. *Geothermal Energy*. 2018;6(1). https://doi.org/10.1186/s40517-018-0114-3.
18. Yoon JS, Zimmermann G, Zang A. Numerical investigation on stress shadowing in fluid injection-induced fracture propagation in naturally fractured geothermal reservoirs. *Rock Mech Rock Eng*. 2015;48(4):1439–1454. https://doi.org/10.1007/s00603-014-0695-5.
19. Hofmann H, et al. First field application of cyclic soft stimulation at the Pohang Enhanced Geothermal System site in Korea. *Geophys J Int*. 2019;217(2):926–949. https://doi.org/10.1093/gji/ggz058.
20. Niemz P, et al. Full-waveform-based characterization of acoustic emission activity in a mine-scale experiment: a comparison of conventional and advanced hydraulic fracturing schemes. *Geophys J Int*. 2020;222(1):189–206. https://doi.org/10.1093/gji/ggaa127.
21. Hulse DS. *Fracturing Process with Superimposed Cyclic Pressure*. Google Patents; 1959.
22. Zang A, et al. Relaxation damage control via fatigue-hydraulic fracturing in granitic rock as inferred from laboratory-, mine-, and field-scale experiments. *Sci Rep*. 2021;11(1):6780. https://doi.org/10.1038/s41598-021-86094-5.
23. Lu G, et al. Time-dependent hydraulic fracture initiation. *J Geophys Res Solid Earth*. 2020;125(3). https://doi.org/10.1029/2019JB018797.
24. Rao M, Ramana YV. A study of progressive failure of rock under cyclic loading by ultrasonic and AE monitoring techniques. *Rock Mech Rock Eng*. 1992;25(4):237–251. https://doi.org/10.1007/bf01041806.

25. Zhuang L, et al. Cyclic hydraulic fracturing of pocheon granite cores and its impact on breakdown pressure, acoustic emission amplitudes and injectivity. *Int J Rock Mech Min Sci.* 2019;122. https://doi.org/10.1016/j.ijrmms.2019.104065.
26. Jia Y, et al. Laboratory characterization of cyclic hydraulic fracturing for deep shale application in Southwest China. *Int J Rock Mech Min Sci.* 2021;148, 104945. https://doi.org/10.1016/j.ijrmms.2021.104945.
27. Patel SM, Sondergeld CH, Rai CS. Laboratory studies of hydraulic fracturing by cyclic injection. *Int J Rock Mech Min Sci.* 2017;95:8–15. https://doi.org/10.1016/j.ijrmms.2017.03.008.
28. Jung S, et al. Fatigue behavior of granite subjected to cyclic hydraulic fracturing and observations on pressure for fracture growth. *Rock Mech Rock Eng.* 2021:1–14. https://doi.org/10.1007/s00603-021-02383-5.
29. Zang A, et al. Hydraulic fracture monitoring in hard rock at 410 m depth with an advanced fluid-injection protocol and extensive sensor array. *Geophys J Int.* 2017;208(2):790–813. https://doi.org/10.1093/gji/ggw430.
30. Moghaddam RH, Golshani A. Experimental study on fracture propagation in anisotropy rock under cyclic hydraulic fracturing. *Eng Fract Mech.* 2024;295, 109775. https://doi.org/10.1016/j.engfracmech.2023.109775.
31. Zhuang L, Zang A. Laboratory hydraulic fracturing experiments on crystalline rock for geothermal purposes. *Earth Sci Rev.* 2021;216, 103580. https://doi.org/10.1016/j.earscirev.2021.103580.
32. Li Z, Elsworth D, Wang C. Constraining maximum event magnitude during injection-triggered seismicity. *Nat Commun.* 2021;12(1):1528. https://doi.org/10.1038/s41467-020-20700-4.
33. Zhuang L, et al. Comparison of fatigue hydraulic fracturing of granite cores subjected to creep and cyclic injection. *Rock Mech Rock Eng.* 2024:1–17. https://doi.org/10.1007/s00603-024-03870-1.
34. Lecampion B, Bunger A, Zhang X. Numerical methods for hydraulic fracture propagation: a review of recent trends. *J Nat Gas Sci Eng.* 2018;49:66–83. https://doi.org/10.1016/j.jngse.2017.10.012.
35. Zhu G, Dong S. Discrete element simulation model of pulsating hydraulic fracturing considering fatigue damage. *Geomech Geophys Geo-Energy Geo-Resour.* 2022;8(4):119. https://doi.org/10.1007/s40948-022-00424-z.
36. Chen Z, Wang M. Pore-scale modeling of hydromechanical coupled mechanics in hydrofracturing process. *J Geophys Res Solid Earth.* 2017;122(5):3410–3429. https://doi.org/10.1002/2017JB013989.
37. Chen B, et al. A review of hydraulic fracturing simulation. *Arch Comput Methods Eng.* 2022;29(4):1–58. https://doi.org/10.1007/s11831-021-09653-z.
38. Mohammadpour A, Paluszny A, Zimmerman R. A robust 3D finite element framework for monolithically coupled thermo-hydro-mechanical analysis of fracture growth with frictional contact in porous media. *Comput Methods Appl Mech Eng.* 2025;434, 117557. https://doi.org/10.1016/j.cma.2024.117557.
39. Mohammadnejad T, Khoei AR. Hydro-mechanical modeling of cohesive crack propagation in multiphase porous media using the extended finite element method. *Int J Numer Anal Methods GeoMech.* 2013;37(10):1247–1279. https://doi.org/10.1002/nag.2079.
40. Jiao YY, et al. A two-dimensional coupled hydromechanical discontinuum model for simulating rock hydraulic fracturing. *Int J Numer Anal Methods GeoMech.* 2015;39(5):457–481. https://doi.org/10.1002/nag.2314.
41. Li SB, Firoozabadi A, Zhang DX. Hydromechanical modeling of nonplanar three-dimensional fracture propagation using an iteratively coupled approach. *J Geophys Res Solid Earth.* 2020;125(8). https://doi.org/10.1029/2020jb020115.
42. Li H, et al. A hydro-mechanical-damage fully coupled cohesive phase field model for complicated fracking simulations in poroelastic media. *Comput Methods Appl Mech Eng.* 2022;399. https://doi.org/10.1016/j.cma.2022.115451.
43. Feng YX, Haugen K, Firoozabadi A. Phase-Field simulation of hydraulic fracturing by CO2, water and nitrogen in 2D and comparison with laboratory data. *J Geophys Res Solid Earth.* 2021;126(11). https://doi.org/10.1029/2021jb022509.
44. Santillán D, Juanes R, Cueto-Felgueroso L. Phase field model of hydraulic fracturing in poroelastic media: fracture propagation, arrest, and branching under fluid injection and extraction. *J Geophys Res Solid Earth.* 2018;123(3):2127–2155. https://doi.org/10.1002/2017jb014740.
45. Chen B, et al. Phase-field simulation of hydraulic fracturing with a revised fluid model and hybrid solver. *Eng Fract Mech.* 2020;229, 106928. https://doi.org/10.1016/j.engfracmech.2020.106928.
46. Sun Y, et al. Investigation of hydraulic fracture branching in porous media with a hybrid finite element and peridynamic approach. *Theor Appl Fract Mech.* 2021;116, 103133. https://doi.org/10.1016/j.tafmec.2021.103133.
47. Sun H, et al. An extended numerical manifold method for two-phase seepage-stress coupling process modelling in fractured porous medium. *Comput Methods Appl Mech Eng.* 2022;391. https://doi.org/10.1016/j.cma.2021.114514.
48. Wang T, et al. Simulation of hydraulic fracturing using particle flow method and application in a coal mine. *Int J Coal Geol.* 2014;121:1–13. https://doi.org/10.1016/j.coal.2013.10.012.
49. Ishida T, et al. Influence of fluid viscosity on the hydraulic fracturing mechanism. *J Energy Resour Technol.* 2004;126(3):190–200. https://doi.org/10.1115/1.1791651.
50. Falls S, et al. Ultrasonic tomography and acoustic emission in hydraulically fractured Lac du Bonnet grey granite. *J Geophys Res Solid Earth.* 1992;97(B5):6867–6884. https://doi.org/10.1029/92JB00041.
51. Yoon JS, Zang AN, Stephansson O. Numerical investigation on optimized stimulation of intact and naturally fractured deep geothermal reservoirs using hydro-mechanical coupled discrete particles joints model. *Geothermics.* 2014;52:165–184. https://doi.org/10.1016/j.geothermics.2014.01.009.
52. Zhang FS, Damjanac B, Huang HY. Coupled discrete element modeling of fluid injection into dense granular media. *J Geophys Res Solid Earth.* 2013;118(6):2703–2722. https://doi.org/10.1002/jgrb.50204.
53. Zhu WW, et al. Numerical investigation of influential factors in hydraulic fracturing processes using coupled discrete element-lattice boltzmann method. *J Geophys Res Solid Earth.* 2023;128(9). https://doi.org/10.1029/2023jb027292.
54. Zhao Q, et al. Numerical simulation of hydraulic fracturing and associated microseismicity using finite-discrete element method. *J Rock Mech Geotech Eng.* 2014;6(6):574–581. https://doi.org/10.1016/j.jrmge.2014.10.003.
55. Lisjak A, et al. A 2D, fully-coupled, hydro-mechanical, FDEM formulation for modelling fracturing processes in discontinuous, porous rock masses. *Comput Geotech.* 2017;81:1–18. https://doi.org/10.1016/j.compgeo.2016.07.009.
56. Wasantha PLP, Konietzky H. Fault reactivation and reservoir modification during hydraulic stimulation of naturally-fractured reservoirs. *J Nat Gas Sci Eng.* 2016;34:908–916. https://doi.org/10.1016/j.jngse.2016.07.054.
57. Zangeneh N, Eberhardt E, Bustin RM. Investigation of the influence of natural fractures and in situ stress on hydraulic fracture propagation using a distinct-element approach. *Can Geotech J.* 2015;52(7):926–946. https://doi.org/10.1139/cgj-2013-0366.
58. Zhao XY, et al. Controls of natural fractures on the texture of hydraulic fractures in rock. *J Petrol Sci Eng.* 2018;165:616–626. https://doi.org/10.1016/j.petrol.2018.02.047.
59. Xi X, et al. Modelling rock fracture induced by hydraulic pulses. *Rock Mech Rock Eng.* 2021;54(8):3977–3994. https://doi.org/10.1007/s00603-021-02477-0.
60. Potyondy DO, Cundall PA. A bonded-particle model for rock. *Int J Rock Mech Min Sci.* 2004;41(8):1329–1364. https://doi.org/10.1016/j.ijrmms.2004.09.011.
61. Itasca. *UDEC (Universal Distinct Element Code), Version 6.0.* Minneapolis, MN, USA: Itasca; 2014.
62. Lan HX, Martin CD, Hu B. Effect of heterogeneity of brittle rock on micromechanical extensile behavior during compression loading. *J Geophys Res Solid Earth.* 2010;115. https://doi.org/10.1029/2009jb006496.
63. Park JW, et al. Polygonal grain-based distinct element modeling for mechanical behavior of brittle rock. *Int J Numer Anal Methods GeoMech.* 2017;41(6):880–898. https://doi.org/10.1002/nag.2634.
64. Wang X, Cai M. A comprehensive parametric study of grain-based models for rock failure process simulation. *Int J Rock Mech Min Sci.* 2019;115:60–76. https://doi.org/10.1016/j.ijrmms.2019.01.008.
65. Abdelaziz A, Zhao Q, Grasselli G. Grain based modelling of rocks using the combined finite-discrete element method. *Comput Geotech.* 2018;103:73–81. https://doi.org/10.1016/j.compgeo.2018.07.003.
66. Choi SO, Chung S-K. Stability analysis of jointed rock slopes with the Barton-Bandis constitutive model in UDEC. *Int J Rock Mech Min Sci.* 2004;41:581–586. https://doi.org/10.1016/j.ijrmms.2004.03.103.
67. Coetzee CJ. Calibration of the discrete element method. *Powder Technol.* 2017;310:104–142. https://doi.org/10.1016/j.powtec.2017.01.015.
68. Al-Busaidi A, Hazzard J, Young R. Distinct element modeling of hydraulically fractured Lac du Bonnet granite. *J Geophys Res Solid Earth.* 2005;110(B6). https://doi.org/10.1029/2004JB003297.
69. Witherspoon PA, et al. Validity of cubic law for fluid-flow in a deformable rock fracture. *Water Resour Res.* 1980;16(6):1016–1024. https://doi.org/10.1029/WR016i006p01016.
70. Zimmerman RW, Bodvarsson GS. Hydraulic conductivity of rock fractures. *Transport Porous Media.* 1996;23:1–30. https://doi.org/10.1007/BF00145263.
71. Okui Y, Horii H. Stress and time-dependent failure of brittle rocks under compression: a theoretical prediction. *J Geophys Res Solid Earth.* 1997;102(B7):14869–14881. https://doi.org/10.1029/97JB00476.
72. Potyondy DO. Simulating stress corrosion with a bonded-particle model for rock. *Int J Rock Mech Min Sci.* 2007;44(5):677–691. https://doi.org/10.1016/j.ijrmms.2006.10.002.
73. Wang MZ, Cai M. A grain-based time-to-failure creep model for brittle rocks. *Comput Geotech.* 2020;119. https://doi.org/10.1016/j.compgeo.2019.103344.
74. Aydan Ö, et al. ISRM suggested methods for determining the creep characteristics of rock. *Rock Mech Rock Eng.* 2014;47(1):275–290. https://doi.org/10.1007/s00603-013-0520-6.
75. Lajtai EZ, Bielus LP. Stress-Corrosion cracking of Lac Du Bonnet Granite in tension and compression. *Rock Mech Rock Eng.* 1986;19(2):71–87. https://doi.org/10.1007/bf01042525.
76. Schmidtke RH, Lajtai EZ. The long-term strength of Lac Du Bonnet granite. *Int J Rock Mech Min Sci.* 1985;22(6):461–465. https://doi.org/10.1016/0148-9062(85)90010-5.
77. Liu G, Cai M. Modeling time-dependent deformation behavior of brittle rock using grain-based stress corrosion method. *Comput Geotech.* 2020;118. https://doi.org/10.1016/j.compgeo.2019.103323.
78. Zhuang L, et al. Effect of water infiltration, injection rate and anisotropy on hydraulic fracturing behavior of granite. *Rock Mech Rock Eng.* 2019;52(2):575–589. https://doi.org/10.1007/s00603-018-1431-3.
79. Nyquist H. Certain topics in telegraph transmission theory. *Transac American Instit Electr Engineers.* 1928;47(2):617–644. https://doi.org/10.1109/T-AIEE.1928.5055024.
80. Min K-B, et al. Stress-dependent permeability of fractured rock masses: a numerical study. *Int J Rock Mech Min Sci.* 2004;41(7):1191–1210. https://doi.org/10.1016/j.ijrmms.2004.05.005.
81. Cerfontaine B, Collin F. Cyclic and fatigue behaviour of rock materials: review, interpretation and research perspectives. *Rock Mech Rock Eng.* 2018;51(2):391–414. https://doi.org/10.1007/s00603-017-1337-5.

82. Yoon JS, Zimmermann G, Zang A. Numerical investigation on stress shadowing in fluid injection-induced fracture propagation in naturally fractured geothermal reservoirs. *Rock Mech Rock Eng*. 2015;48:1439–1454. https://doi.org/10.1007/s00603-014-0695-5.
83. Clarke H, et al. Felt seismicity associated with shale gas hydraulic fracturing: the first documented example in Europe. *Geophys Res Lett*. 2014;41(23):8308–8314. https://doi.org/10.1002/2014GL062047.
84. Stanĕk F, Eisner L. Seismicity induced by hydraulic fracturing in shales: a bedding plane slip model. *J Geophys Res Solid Earth*. 2017;122(10):7912–7926. https://doi.org/10.1002/2017JB014213.
85. Tary J-B, Van der Baan M, Eaton DW. Interpretation of resonance frequencies recorded during hydraulic fracturing treatments. *J Geophys Res Solid Earth*. 2014;119(2):1295–1315. https://doi.org/10.1002/2013JB010904.
86. Sobhaniaragh B, et al. The role of stress interference in hydraulic fracturing of horizontal wells. *Int J Rock Mech Min Sci*. 2018;106:153–164. https://doi.org/10.1016/j.ijrmms.2018.04.024.
87. Escobar RG, et al. Xfem modeling of stress shadowing in multiple hydraulic fractures in multi-layered formations. *J Nat Gas Sci*. 2019;70, 102950. https://doi.org/10.1016/j.jngse.2019.102950.
88. Vogler D, et al. Permeability evolution in natural fractures subject to cyclic loading and gouge formation. *Rock Mech Rock Eng*. 2016;49:3463–3479. https://doi.org/10.1007/s00603-016-1022-0.
89. Scholz CH. Static fatigue of quartz. *J Geophys Res*. 1972;77(11):2104. https://doi.org/10.1029/JB077i011p02104.
90. Westaway R, Burnside NM. Fault "Corrosion" by Fluid Injection: a Potential Cause of the November 2017 MW 5.5 Korean earthquake. *Geofluids*. 2019. https://doi.org/10.1155/2019/1280721, 2019.